ACS APPLIED MATERIALS & INTERFACES

Research Article

www.acsami.org

Plasma-Induced Oxygen Vacancies in Ultrathin Hematite Nanoflakes Promoting Photoelectrochemical Water Oxidation

Changqing Zhu,[†,‡,#] Changli Li,[‡,#] Maojun Zheng,[†] and Jean-Jacques Delaunay*[,‡]

[†]Department of Physics and Astronomy, Shanghai Jiao Tong University, Shanghai 200240, PR China

[‡]School of Engineering, The University of Tokyo, 7-3-1 Hongo, Bunkyo-ku, Tokyo 113-8656, Japan

Supporting Information

ABSTRACT: The incorporation of oxygen vacancies in hematite has been investigated as a promising route to improve oxygen evolution reaction activity of hematite photoanodes used in photoelectrochemical water oxidation. However, introducing oxygen vacancies intentionally in α-Fe_2O_3 for active solar water splitting through facile and effective methods remains a challenge. Herein, air plasma treatment is shown to produce oxygen vacancies in α-Fe_2O_3, and ultrathin α-Fe_2O_3 nanoflakes are used to investigate the effect of oxygen vacancies on the performance of photoelectrochemical oxygen oxidation. Increasing the plasma treatment duration and power is found to increase the density of oxygen vacancies and leads to a significant enhancement of the photocurrent response. The nanoflake photoanode with the optimized plasma treatment yields an incident photo-to-current conversion efficiency of 35.4% at 350 nm under 1.6 V vs RHE without resorting to any other cocatalysts, an efficiency far exceeding that of the pristine α-Fe_2O_3 nanoflakes (~2.2%). Evidence for the presence of high density of oxygen vacancies confined in nanoflakes is clarified by X-ray photoelectron spectroscopy. The increased number of oxygen vacancies after plasma treatment resulting in an increased carrier density is interpreted as the main cause for the enhanced oxygen evolution reaction activity.

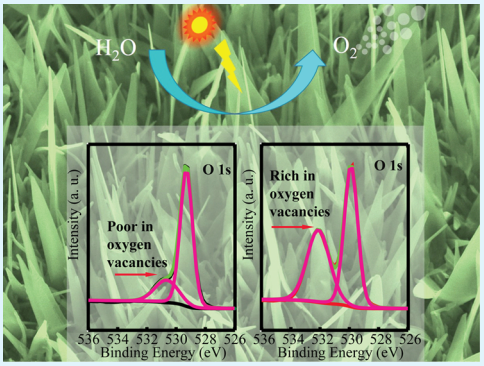

KEYWORDS: *hematite, nanoflakes, plasma treatment, oxygen vacancies, photoelectrochemical water oxidation*

INTRODUCTION

Photoelectrochemical water splitting is a promising way to convert solar energy into chemical energy in the form of storable hydrogen.[1−3] Using low-cost metal-oxide semiconductors to realize photoelectrochemical water splitting has attracted much attention in recent years. Among possible semiconductor materials for solar water splitting, hematite offers decisive advantages such as a suitable band gap for sun light absorption (~2.2 eV) and being earth abundant, nontoxic, and chemically stable under photoanodic conditions.[4−6] Hematite theoretical solar-to-hydrogen efficiency can be as large as 16.8% under solar irradiation (AM 1.5G illumination, 100 mW/cm^2) at 1.23 V vs RHE, generating a photocurrent density of 12.6 mA cm^{-2}.[4,6]

However, the performance of the produced hematite photoanodes being limited by many factors remains low with solar-to-hydrogen efficiency below 2%.[7,8] The short hole diffusion length (2−4 nm) and long photon penetration depth in the visible wavelength range render hematite particularly challenging to achieve a balance between efficient carrier collection and light absorption.[9] This serious drawback may be addressed by using ultrathin structures or nanostructures,[2,10] in which the thickness of hematite structures should be restricted to less than 50 nm.[10] Ultrathin hematite films can be deposited by atomic layer deposition,[11] spray pyrolysis,[12,13] or other techniques. These ultrathin hematite films without modification show low performance in photoelectrochemical (PEC) water splitting, as the thin film thickness leads to small light absorption. Besides, much effort from utilizing the micro- and nanostructures has been used to decouple the directions of light absorption and photoinduced carrier collection.[2,14−16] For hematite, various nanostructures have been prepared to realize water splitting, including porous nanostructures, nanowires, dendrites, and nanoflakes.[17−20] The combination of nanostructures and doping such as Si,[21,22] Sn,[18,23] Al,[23] Ti,[24−26] Pt,[7,27] Zn,[28] and P[6] was found to improve carrier collection and conductivity and thus enhance the PEC activity of hematite. However, most fabrication methods are based on the combination of a hydrothermal method and a subsequent annealing at high temperature, thus increasing the complexity and cost of the fabrication process.

Recently, oxygen vacancies have been reported to improve the activity of semiconductor photonaodes for water oxidation.[8,29−32] Oxygen vacancies in In_2O_3 porous sheets were shown to increase solar light absorption through narrowing the band gap and also serve as the active sites to improve the carrier separation efficiency, thus finally achieving improved water splitting efficiency.[29] $NiCo_2O_4$ ultrathin

Received: July 8, 2015
Accepted: September 24, 2015
Published: September 24, 2015

© 2015 American Chemical Society

DOI: 10.1021/acsami.5b06131
ACS Appl. Mater. Interfaces 2015, 7, 22355−22363

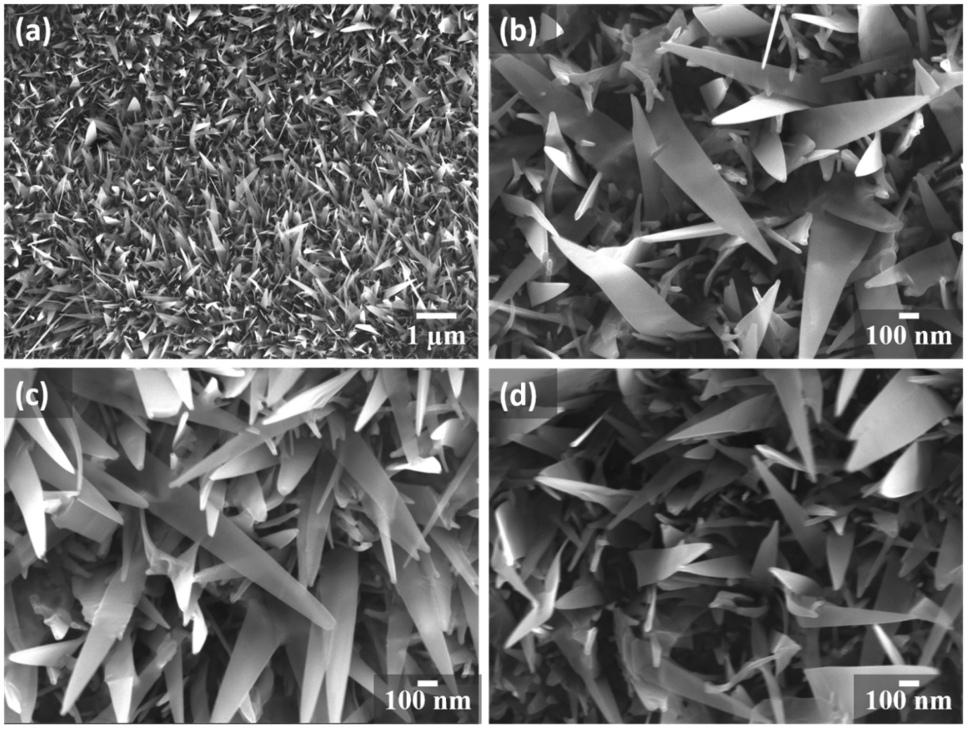

Figure 1. SEM images of the samples showing the nanoflake nanostructures: (a) as-prepared sample annealed at 400 °C for 1 h in air, (b) is a magnified image of (a), (c) after medium power plasma treatment, and (d) after high power plasma treatment.

nanosheets with high-density oxygen vacancies was also found to exhibit a higher oxygen evolution reactivity, benefiting from the lowered adsorption energy of H_2O on the nanosheets.[30] The incorporation of oxygen vacancies has also been shown to be an effective approach to improve the activity of hematite photoelectrodes.[8,33] Through transient absorption spectroscopy analysis, Cowan et al. suggested that the primary effect of introducing oxygen vacancies is to block slow surface hole-bulk electron recombination pathways.[8] Ozin et al. investigated high-temperature treatment of ultrathin film of hematite under an atmosphere of H_2 and Ar and suggested that the generated oxygen vacancies upon high temperature treatment are responsible for the activation of the photoanode by improving the electron collection.[33] Finally, thermal annealing under oxygen-deficient atmosphere of hematite was reported as an efficient means to control oxygen vacancy density, which was used to increase the photocurrent of hematite photoanodes.[34,35]

Herein, we combine a low-temperature fabrication technique of ultrathin hematite nanoflakes with a plasma post-treatment to control the density of oxygen vacancies and investigate the effect of oxygen vacancies on photocatalysis with the aim of realizing high photoactivity for nanostructured hematite photoanodes. The ultrathin nanoflakes provide a short path length for hole diffusion, and the self-standing array of nanoflake structures enhances light absorption due to light scattering by the nanostructures. Thus, the pristine hematite nanoflakes prepared with the low temperature process provide an excellent two-dimensional nanostructure to decouple the directions of light absorption and photogenerated carrier collection. A relatively low power plasma treatment is used so that surface activation of the nanoflakes is obtained while maintaining the nanoflake morphology. Intentionally incorporated oxygen vacancies during the plasma treatment activate the electrochemically active sites on the nanoflakes to promote the photoactivity of the hematite photoanode.

EXPERIMENTAL SECTION

Preparation of Hematite Nanoflakes. For the preparation of the hematite nanoflakes, high pure quality (99.99%) iron foils with a thickness of 0.2 mm were obtained from Nilaco Corporation. The foil surface was pretreated by mechanical polishing and then cut into 6 × 10 mm^2 pieces. For comparison purposes, foils without polishing were also used. The foils were degreased by successively sonicating them for 10 min in acetone and ethanol. Then the foils were rinsed at least three times in deionized water and dried by blowing dry air. The foils were placed in the center of an alumina crucible and then sintered in a muffle furnace (Yamato, FO100). The temperature was increased with a rate of 10 °C per minute until it reached the sintering temperature of 400 °C and maintained at 400 °C for 1 h. After natural cooling of the muffle furnace, the samples were treated in plasma. The plasma treatment was performed using a plasma cleaner (Harrick PDC-32G) equipped with a radio frequency coil with adjustable power. The plasma treatment was performed for the two available plasma powers, namely a medium power of 10.5 W (PM) and a high power of 18 W (PH). The effect of the plasma treatment duration (4, 10, 15, 20, 25, 30 min for PM and 5, 15, 25, 35, 45 min for PH) was also investigated. The samples are referred to "as-prepared" for the samples obtained after the sintering process and "PM" and "PH" for the plasma treated samples using the available medium power and high power, respectively.

Additional deposition of Co-Pi on the surface of the PH sample was performed using photoassisted electrodeposition.[36,37] The Co-Pi cocatalyst was deposited in a stirred solution of 0.5 mM $Co(NO_3)_2$ in 0.1 M KPi buffer at pH 7. A 500 W xenon lamp was used as the light source (285 mW/cm^2). Photoassisted electrodeposition was performed at 0.1 V vs Ag/AgCl for 5 min. The Co-Pi modified sample was finally washed in deionized water.

Structural Characterization. The sample morphology was characterized using a field-emission scanning electron microscope (JEOL JSM 7600FA). The X-ray diffraction (XRD) data was acquired with a Rigaku Miniflex II-MW in both Bragg−Brentano (theta-2theta)

DOI: 10.1021/acsami.5b06131
ACS Appl. Mater. Interfaces 2015, 7, 22355−22363

and grazing incidence (detector scan) modes using the Cu Kα radiation. The XRD spectra were acquired for the 2θ range of 25−65° with a scan step of 0.02° and a scan speed of 1° per minute. Raman spectra were recorded at room temperature on a Renishaw inVia Raman Microscope system with a 488 nm excitation light (0.82 mW) directed through a ×100 objective. The UV−vis diffuse reflectance spectra were measured with a spectrophotometer equipped with an integrating sphere (V-560 and DRS, JASCO). X-ray photoelectron spectroscopy (XPS) spectra were collected with a PHI 5000 VersaProbe (ULVAC-PHI) using an Al Kα X-ray source (1486.6 eV). The electron analyzer was operated at pass energies of 117.4 eV for the wide scans and 23.5 eV for the narrow scans.

Photoelectrochemical Measurement. Photoelectrochemical water splitting performance of the fabricated photoelectrodes were obtained using a three-electrode cell. The nanoflake structured photoanodes were used as the working electrode, Pt wire as the counter electrode, and Ag/AgCl electrode as the reference electrode. The potential of the working electrode was controlled with a potentiostat (VersaSTAT 4, Princeton Applied Research). The measured potentials vs Ag/AgCl were converted to the reversible hydrogen electrode (RHE) scale according to the relationship $E_{RHE} = E_{Ag/AgCl} + 0.059\ pH + E^0_{Ag/AgCl}$, where $E_{Ag/AgCl}$ is the measured potential against the reference electrode and $E^0_{Ag/AgCl} = 0.1976$ V at 25 °C. An aqueous solution of 1 M NaOH (pH 13.6) was used as the electrolyte. The electrolyte was stirred and purged with Ar gas for 15 min before the measurements. The fabricated hematite photoanodes were illuminated with a 500 W xenon lamp delivering an irradiance of 285 mW/cm^2 on the photoanodes. The scan rate was 10 mV/s for the current−potential (J-E) curves, and the scans were performed from negative to positive potentials. When the incident photon conversion efficiency (IPCE) was measured, the photoanodes were illuminated using the same light source, which was filtered using bandpass filters (full width at half-maximum of 38 ± 2 nm) having center wavelengths of 350, 400, 450, 500, and 550 nm. The IPCE measurements were carried out at 1.23 and 1.6 V vs RHE. The IPCEs were calculated for each center wavelength using the equation $IPCE = [(1240/\lambda) \times (J_{light} - J_{dark})/P_{light}] \times 100\%$, where J_{light} is the steady-state photocurrent density at a specific wavelength, J_{dark} is the dark current density, λ is the wavelength of the incident light, and P_{light} is the light intensity at the corresponding wavelength.

The Mott−Schottky and electrochemical impedance spectroscopy (EIS) measurements were performed using the same electrochemical measurement system as for the PEC measurements. Mott−Schottky measurements were obtained under dark conditions at a frequency of 1000 Hz in 1 M NaOH (pH 13.6) solution with a scan rate of 10 mV/s. EIS measurements were performed at an applied potential of 1.8 V vs RHE in dark for a frequency range between 100,000 and 1 Hz using 10 mV amplitude sinusoidal perturbation.

RESULTS AND DISCUSSION

Figure 1 (a) shows the SEM image of the as-prepared sample obtained by annealing the Fe foil in the muffle furnace at 400 °C for 1 h. A uniform coverage of nanoflakes was obtained upon annealing of the Fe foil. Figure 1 (b) shows a high magnification image of the nanoflakes on the as-prepared sample. The nanoflakes have a thickness of approximately 20−30 nm and a length of 1−2 μm. It should be noted that prepolishing of the Fe foil annealing is necessary to obtain uniformly distributed nanoflakes. Without polishing, the sample observed after annealing exhibited a sparse distribution of nanoflakes, as shown in Figure S1. This may be explained by the presence of a passivation layer (native oxide layer) formed on the surface of the as-received Fe foils and the removal of the passivation layer by polishing, resulting in a uniform growth of nanoflakes on the pure iron layer. The effect of the plasma treatments on the sample morphology is examined using SEM images of plasma treated samples for 25 min. Figure 1 (c) and (d) displays the SEM images for the PM and PH samples. When compared to the morphology of the as-prepared nanoflakes, the PM and PH samples show no obvious change. The plasma treatment used in this report did not deteriorate the nanostructures of the as-prepared samples, thus providing a method for surface treatment of low-dimensional nanostructures on a sample surface.

The XRD measurement in the Bragg−Brentano configuration for the as-prepared nanoflakes and the sample treated with medium power plasma is shown in Figure S2. All XRD peaks of Figure S2 were indexed to magnetite and iron. In the case of Fe foil annealing under high temperatures, a multilayered oxide coating is usually formed on the surface of the iron foil, consisting of hematite as the outer layer, Fe_3O_4 as the intermediate layer, and FeO as the inner layer in direct contact with the iron substrate.[38,39] The formation of hematite and magnetite can be summarized as follows:[40,41]

$$2Fe + O_2 \rightarrow 2FeO$$

$$6FeO + O_2 \rightarrow 2Fe_3O_4$$

$$4Fe_3O_4 + O_2 \rightarrow 6Fe_2O_3$$

The decreased oxygen content along the depth of the multilayered oxide coating (from the oxide top surface to the Fe substrate) may account for the formation of the Fe_3O_4 phase during thermal oxidation.[31,34,35,42] Additional information about the phase of the nanostructures forming the sample top surface is obtained using X-ray diffraction (XRD) patterns performed with a grazing incidence angle of 0.5°. The XRD spectra presented in Figure 2 (a) show that all samples contain

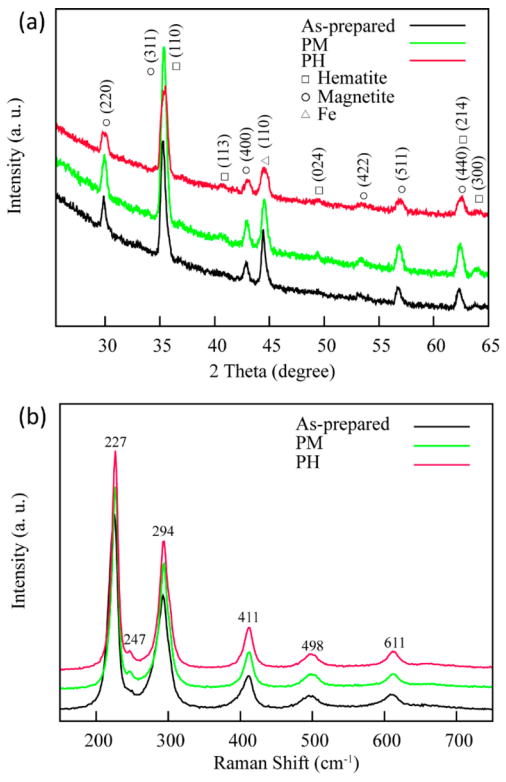

Figure 2. (a) XRD spectra performed with grazing angle incidence collected for the as-prepared, medium power (PM) and high power (PH) plasma treatments. (b) Raman spectra for the as-prepared, PM and PH samples.

DOI: 10.1021/acsami.5b06131
ACS Appl. Mater. Interfaces 2015, 7, 22355−22363

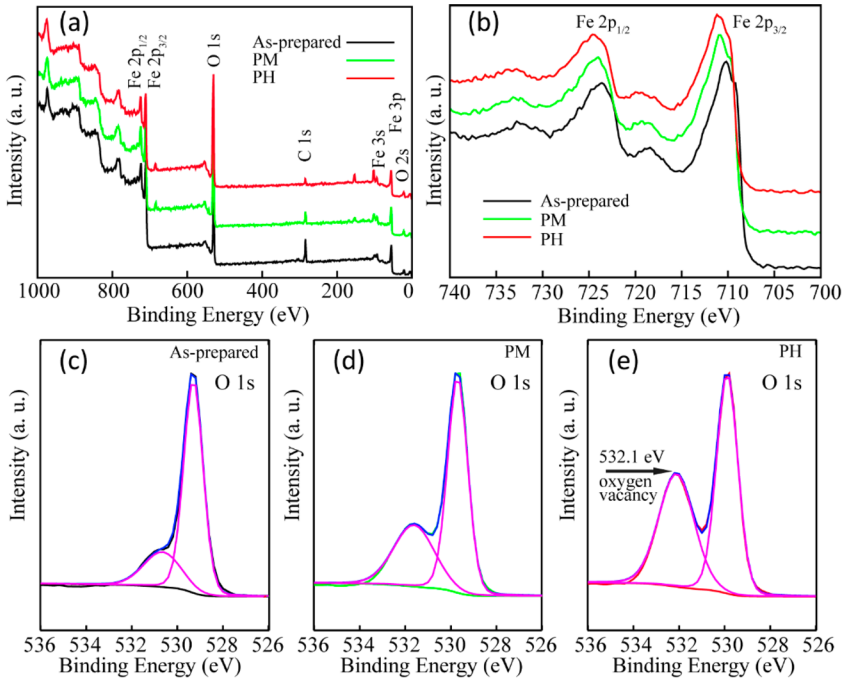

Figure 3. X-ray photoelectron spectroscopy analysis: (a) survey spectra of the as-prepared, PM, and PH samples, (b) Fe 2p peaks of the as-prepared, PM, and PH samples, (c,d,e) O 1s peaks of the as-prepared, PM, and PH samples.

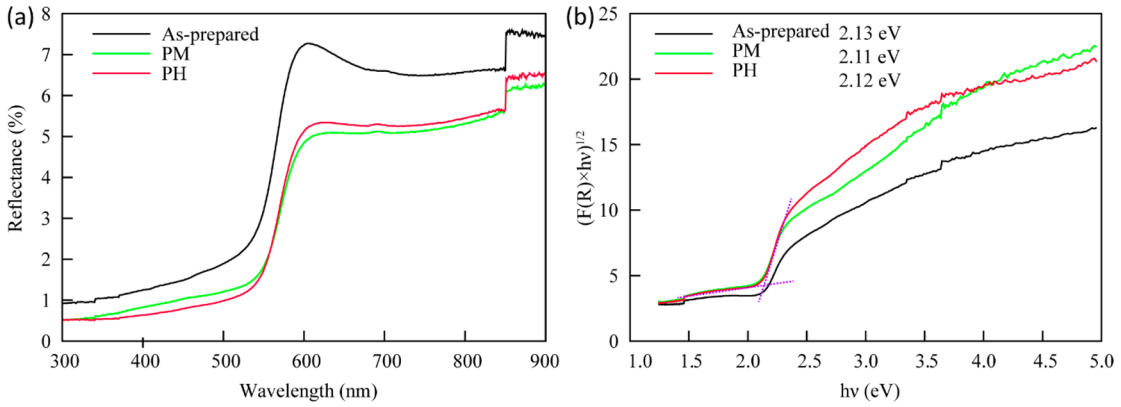

Figure 4. (a) Diffuse reflectance spectra for the as-prepared, PM, and PH samples. (b) Kubelka–Munk plots used to estimate the band gap of the samples.

hematite, magnetite, and iron, a result consistent with the mixed iron oxides formed during thermal oxidization of iron foils.[38] However, the peaks belonging to the hematite phase, indexed as (113), (024), and (300), have weak intensity. The (110) peak of hematite superimposes with that of the (311) magnetite peak. Thus, Raman spectroscopy with a probe light of 488 nm was used to identify the hematite phase since this technique is more sensitive to an absorbing surface phase such as hematite than XRD analysis.[38] Figure 2 (b) shows the Raman spectroscopy measurements for the samples with and without plasma treatments. All samples display the same characteristic hematite peaks: the six peaks of hematite (D^6_{3d} space group) include 227 and 498 cm^{-1} corresponding to the A_{1g} mode and 247, 294, 411, and 611 cm^{-1} attributed to E_g modes.[31,43] From both XRD and Raman results, it is concluded that all samples consist of a top surface layer made of hematite stacked on a magnetite layer.

The Fe oxidation state of the sample surfaces was further examined by XPS, which provides a depth analysis of a few nanometers.[33] Figure 3 summarizes the XPS results for the as-prepared, PM and PH samples. The Fe 2p spectrum of the as-prepared sample (Figure 3 (b)) reveals a typical Fe_2O_3 spectrum having the binding energies of 710.2 eV for Fe $2p_{3/2}$ and 723.6 eV for Fe $2p_{1/2}$, the shakeup satellite located at 718 eV, and the characteristic satellite peaks for the α-Fe_2O_3 or γ-Fe_2O_3 phases.[44−47] Although γ-Fe_2O_3 is reported to exhibit the same Fe 2p core-level spectra with α-Fe_2O_3,[46] the possible presence of the γ-Fe_2O_3 is excluded by the Raman spectra analysis, in which no vibration mode from γ-Fe_2O_3 was found. As seen in Figure 3 (b), the plasma treatment shifts the peak positions of the Fe 2p core levels to higher binding energy: the Fe $2p_{3/2}$ and Fe $2p_{1/2}$ peak positions of the PM and PH samples are 711 and 724 eV and 711.2 and 724.6 eV, respectively. The shift to higher binding energy upon plasma treatment very likely results from the appearance of the Fe(II) oxidation state,[47,48] resulting from the generation of oxygen vacancies. The presence of oxygen vacancies is confirmed by analyzing the O 1s peaks reported in Figure 3 (c), (d), and (e). The observed

DOI: 10.1021/acsami.5b06131
ACS Appl. Mater. Interfaces 2015, 7, 22355−22363

main peak at 529.9 eV (O 1s) is due to oxygen atoms bound to metals,[29,49,50] while the shoulder peak at approximately 532 eV is attributed to the defect sites with a low oxygen coordination, i.e. oxygen vacancies.[29,30,33,51] Deconvolution of the O 1s spectra shows that the intensity of the shoulder peak around 532 eV relative to that of the main oxide peak at 529.9 eV increases from 0.46, 0.78, to 1.00 for the as-prepared, PM, and PH samples, respectively. These results indicate that plasma treatment introduces oxygen vacancies into the hematite nanoflakes, and the increase in the plasma power results in a higher density of oxygen vacancies. The vacancy formation mechanism may involve direct removal of oxygen from the hematite lattice by the plasma energetic species and also removal of oxygen assisted by local heating under the oxygen-deficient atmosphere. The oxygen vacancies ionized the hematite lattice, thus generating electrons in the conduction band:[34,52]

$$O_O^x \rightarrow \frac{1}{2}O_2(g) + V_O^{\cdot\cdot} + 2e^-$$

This result is important because it provides a means to control the amount of oxygen vacancies, which have been reported to play an important role in the oxygen evolution reaction.[29,30,33] In summary, a rational and effective introduction of oxygen vacancies into hematite nanoflakes using a simple plasma treatment was demonstrated and has potential contribution toward enhanced photo-electro-oxidation catalysis.

Figure 4 (a) shows the UV–vis diffuse reflectance spectra of the samples. The α-Fe_2O_3 nanoflakes exhibited a clear absorption edge around 600 nm, in agreement with the characteristic absorption edge of hematite in the literature.[9,33] All three samples showed similar optical properties from the ultraviolet to the visible region. The reflectance spectra showed a very low reflectance which may be attributed to the nanostructured morphology enhancing light trapping. The absorption of solar radiation with a wavelength smaller than 600 nm could be used to excite the photogenerated carriers, enabling an effective utilization of visible solar radiation in PEC water splitting reaction. In order to evaluate the band gap energy of the samples, $(F(R) \times h\nu)^{1/2}$ values for an indirect band gap material[53] were plotted versus excitation energy as shown in Figure 4 (b). The absorption coefficient $F(R)$ was calculated according to the Kubelka–Munk (K–M) equation[54,55]

$$F(R) = \frac{(1-R)^2}{2R} \quad (1)$$

where R is the sample reflectance. The band gaps are estimated to be 2.13, 2.11, and 2.12 eV, for the as-prepared, PM, and PH samples, respectively.

The linear scan voltammetry (LSV) results taken in 1 M NaOH (pH 13.6) electrolyte at a scan rate of 10 mV/s under a Xe lamp are presented in Figure 5. The as-prepared sample yielded a relatively low photocurrent density of 0.17 mA/cm^2 at 1.23 V vs RHE. After the medium power plasma treatment (PM for a 25 min plasma treatment), the photocurrent density was enhanced by a factor of ~7.6, reaching 1.30 mA/cm^2 at 1.23 V vs RHE. The photoactivity is found to increase with the plasma treatment duration, and the photoactivity improvement reached a plateau after 25 min of treatment (Figure S3), a duration corresponding to the optimum performance. Increasing the power of the plasma (PH for 25 min) resulted in further improvement of the photoactivity. Indeed, the photocurrent

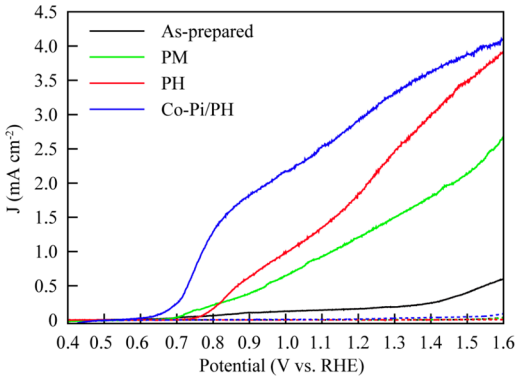

Figure 5. *J-E* curves for the as-prepared, PM and PH samples under 500 W Xe lamp (285 mW/cm^2) illumination (solid lines) and dark condition (dashed lines) in 1 M NaOH (pH 13.6).

density reached 2.03 mA/cm^2 at 1.23 V, achieving an enhancement factor of ~12 with respect to the as-prepared sample. The high power plasma treatment is also found to be more effective, as a 5 min PH treatment lead to a photocurrent higher than that of the 25 min PM treatment. The PH treatment improvement saturates at about 25 min (Figure S4) and shows an increase in the photocurrent at more positive applied voltages. Moreover, it is found that the plasma enhanced photoactivity is strongly dependent on the sample morphology, the best results being achieved for a high density of nanoflakes. Samples prepared without prepolishing of the iron foil lead to the formation of sparse distribution of nanoflakes, whereas applying a prepolishing process results in a uniform and dense distribution of nanoflakes in a reproducible manner. The photocurrent comparison between the sparse and dense nanoflake samples after PH treatment reveals a much larger current for the dense nanoflake sample (Figure S5). This result proves that the two-dimensional nanoflakes standing on the sample surface provide a unique platform for PEC performance enhancement due to the possible creation of a large number of electrochemically active sites and the decrease in the diffusion path length of the minority carriers.[29,30]

It is also noted that the plasma treatment shifts the onset potential toward more positive potentials. The onset potential for the as-prepared sample of 0.55 V increased to 0.65 and 0.7 V for the PM and PH treatments, respectively. The adverse positive shift of the onset potential suggesting limited kinetics for water oxidation likely originated in the increase in the surface trapping states as a result of the plasma treatment. Oxygen vacancies produced by the hydrogen treatment have been reported to act as surface trapping states.[33] Co-catalysts are widely used for facilitating the interfacial water oxidation, so that cocatalysts can remediate the overpotential resulting from the plasma treatment. Co-Pi is one of the cocatalysts used in combination with hematite. Co-Pi has a brownish color and an absorption coefficient of ~3×10^6 m^{-1}.[56] To ensure that more than 90% of the incident light reaches the hematite layer, the thickness of Co-Pi should be less than 35 nm.[56] According to Co-Pi composition (Co:K:P of 2.7:1:1) and mass density (3 g/cm^3), and assuming that all charges were used to oxidize Co^{2+} in the solution to Co^{3+} in Co-Pi,[56,57] the Co-Pi deposited thickness on the hematite photoanode was estimated to be less than 20 nm (total charge density of 4.7 mC/cm^2). For this small thickness, no important change in the optical properties of the samples coated with Co-Pi should be observed, as evidenced by the reflectance spectra of the PH samples without

DOI: 10.1021/acsami.5b06131
ACS Appl. Mater. Interfaces 2015, 7, 22355–22363

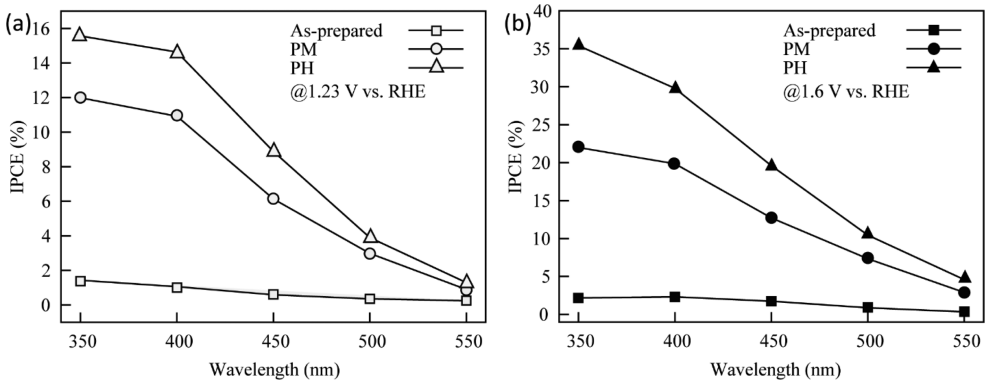

Figure 6. Comparison between the IPCEs of the as-prepared, PM, and PH samples measured at (a) 1.23 V vs RHE and (b) 1.6 V vs RHE. The electrolyte was 1 M NaOH (pH 13.6).

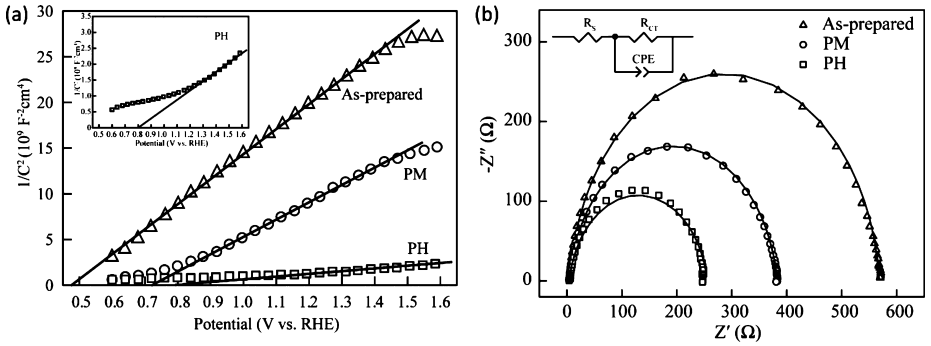

Figure 7. Mott–Schottky plots (a) and Nyquist plots (b) for the as-prepared, PM, and PH samples obtained in 1 M NaOH electrolyte (pH 13.6) under dark conditions. Inset (a): enlarged Mott–Schottky plot for the PH sample. Inset (b): the equivalent circuit used for fitting the experimental data.

and with Co-Pi deposition (Figure S6). Thus, the Co-Pi coating conditions should ensure that most incident light reaches the hematite layer of the photoanode. As shown in Figure 5, deposition of "Co-Pi" cocatalyst on the surface of the PH sample drastically shifted the onset potential toward negative values (0.55 V was achieved, corresponding to onset potential before plasma treatment), indicating a decreased overpotential and improved kinetics for water oxidation. At the same time, the photocurrent showed a remarkable enhancement over a large potential range (0.6–1.6 V). The photocurrent density reached 1.29 mA/cm^2 at 0.8 V, 3.02 mA/cm^2 at 1.23 V, and the highest photocurrent density of 4.1 mA/cm^2 at 1.6 V vs RHE.

The sample IPCEs with and without plasma treatment measured as a function of wavelength are presented in Figure 6. In contrast to literature results for which high temperature annealing (~800 °C) or doping were used to activate the hematite PEC performance, we show that nanoflakes synthesized at low temperature (~400 °C) can be activated by introducing oxygen vacancies through a plasma treatment. Under 1.23 V vs RHE (Figure 6(a)), the IPCE measured for the as-prepared nanoflakes is 1.43% at λ = 350 nm. The IPCE of PM sample increased to 12% at λ = 350 nm, providing an 8.4-fold increase compared to the as-prepared sample. This result is also higher than the pristine hematite synthesized via hydrothermal method and then annealed at 750 °C.[6] The PH plasma treatment further increases the IPCE to 15.6% at λ = 350 nm, a result comparable to that of the pristine hematite nanowires prepared at 800 °C and even better than the Sn-doped hematite nanocorals fabricated at 650 °C and Sn-doped hematite nanowires.[18,31] Under 1.6 V vs RHE, the highest IPCE of the PH sample was achieved at λ = 350 nm reaching a value of 35.4%, which is 1.6 times that of the PM sample (22% at λ = 350 nm) and 16 times that of the as-prepared sample, as shown in Figure 6(b). At λ = 400 nm, the IPCE of the PH sample (29.8%) is 1.5 times that of the PM sample (19.9%) under 1.6 V. As shown in Figure 6, the PH sample showed higher IPCE values than those of the PM treated and as-prepared samples over the whole region for light absorption. The wavelength dependence of IPCE for the samples was consistent with the absorbance spectrum (Figure 4) and photocurrent densities (Figure 5). The observed enhanced IPCE and photocurrent density for the PH sample could be ascribed to the high density of oxygen vacancies introduced by the plasma treatment.[29,30] Finally, the stability of the plasma treatment was checked by measuring the photocurrent of the photoanodes treated with PM and PH plasma at 1.5 V versus RHE for 20 min (Figures S7 and S8). The constant photocurrent for both PM and PH photoanodes indicated that the incorporated oxygen vacancies were stable.

The pronounced effect of the plasma treatment is further examined with Mott–Schottky measurements. The Mott–Schottky curves of the samples presented in Figure 7 (a) revealed positive slopes, indicating that the samples are n-type semiconductors having holes as minority carriers. In the following, the flatband potential at the sample/solution interface and the sample carrier density are estimated from the Mott–Schottky equation[18]

$$\frac{1}{C^2} = \left(\frac{2}{e\varepsilon_0\varepsilon N_d}\right)\left[(V - V_{fb}) - \frac{kT}{e}\right] \quad (2)$$

DOI: 10.1021/acsami.5b06131
ACS Appl. Mater. Interfaces 2015, 7, 22355–22363

where C is the specific capacitance (F cm^{-2}), e is the electron charge, ε_0 is the permittivity of vacuum, ε is the dielectric constant of hematite ($\varepsilon = 80$),[58,59] N_d is the donor density, V is the applied voltage, V_{fb} is the flatband potential, k_B is the Boltzmann constant, and T is the absolute temperature. Extrapolating the linear region of the Mott−Schottky plots and reading the intercept value on the x-axis give an estimate of the flat band potential (V_{fb}). The V_{fb} of the as-prepared sample was 0.48 V, a value close to another report.[18] For the PM and PH samples, V_{fb} was found to be 0.72 and 0.80 V, respectively. The increase in V_{fb} with the plasma treatment is consistent with the increase in the onset potential observed in LSV measurements.

The donor density is estimated from the slope determined in the Mott−Schottky plots:

$$N_d = \frac{2}{e\varepsilon_0\varepsilon}\left[\frac{d\left(\frac{1}{C^2}\right)}{dV}\right]^{-1} \quad (3)$$

The donor densities of the samples increased from 6.44×10^{19} cm^{-3}, 9.32×10^{19} cm^{-3}, to 6.07×10^{20} cm^{-3} for the as-prepared, PM, and PH samples, respectively (here a relative comparison is provided to study the effect of the plasma treatment at constant sample shape and no correction is made to take into account the sample geometry, for example using the roughness factor[60]). The increase in the carrier density upon plasma treatment is thought to promote the sample conductivity and therefore improve the PEC performance.[6,29,33]

In the following, electrochemical impedance spectroscopy (EIS) under dark conditions is used to investigate the interfacial electrical conductivity of hematite in the electrolyte solution. Fitting the EIS data to equivalent circuits consisting of a combination of resistances and capacitors offers a means to discuss the charge transport. A typical set of data taken under 1.8 V is plotted in Figure 7 (b) in the form of a Nyquist plot. The measured points (symbols) are used to fit curves (solid lines) corresponding to the equivalent circuit (inset of Figure 7 (b)), which consists of a serial resistor (R_S) and an RC circuit. The RC circuit models the parallel combination of the interfacial charge transfer resistance (R_{CT}) and the constant phase element (CPE), attributed to the interface between the photoanode surface and the electrolyte. The charge transfer resistance and double layer capacitance of the samples without and with plasma treatment are listed in Table S1. Compared with the as-prepared hematite nanoflake photoanode, the charge transfer resistance of the samples treated with plasma decreased and the corresponding capacitances increased, indicating that the plasma treatment reduced the charge transfer resistance and improved the capacitance at the photoanode/electrolyte interface, thus enhancing the PEC water splitting performance.

In summary, the improved PEC performance of the hematite nanoflakes treated by plasma treatment is attributed to the increase in the oxygen vacancy density produced during the plasma treatment.[29,33] The ultrathin nanoflake structures developing a large surface area provide more electrochemically active surface sites on the sample surface than flat films, leading to efficient catalysis toward water oxidation. The two-dimensional nanoflake structures with ultrathin thickness (20−30 nm) also help to shorten minority carrier transport length, which may decrease carrier recombination during the water oxidation process.[4] Moreover, it is reported that the introduction of oxygen vacancies in the ultrathin structure can decrease the energy required for the adsorption of water molecules onto the sample surface and thus increase the oxygen evolution reaction rate.[30] Plasma treatment is found to increase the number of oxygen vacancy sites on the surface of hematite nanoflakes. The surface oxygen vacancy sites are favorable for hydroxyl adsorption, thus increasing water adsorption.[61,62] Measurement of the water contact angle of the hematite with and without plasma treatment is discussed in the following. Figure S9 (a) showed that the surface of an as-prepared sample has a water contact angle of ∼118°. Modification of the hematite surface by plasma treatment with medium and high power plasma produced a highly hydrophilic surface with a contact angle of ∼0°, as shown in Figure S9 (b) and (c). In summary, the surface of hematite nanoflakes becomes hydrophilic upon plasma treatment so that improved adsorption of water molecules on the nanoflake surface may contribute to the improvement of the oxygen evolution reaction efficiency.[30] In our results, the introduction of oxygen vacancies in nanoflakes not only improves the water molecules adsorption ability on the sample surface but also increases the carrier density of the samples, resulting in intimate contact with the electrolyte and enhanced PEC activity toward water splitting.

CONCLUSION

Ultrathin hematite nanoflakes forming a nanostructured photoanode were used to investigate the effect of intentionally incorporated oxygen vacancies on the PEC water splitting activity. The nanoflakes were prepared by annealing iron foils at 400 °C in air and were activated using a plasma treatment that generates oxygen vacancies in the hematite nanoflakes. Combining XPS and Mott−Schottky analysis, it is concluded that the increased density of the oxygen vacancies induced by the plasma treatment are responsible for the increase in the carrier density of the photoanode. The optimum plasma treatment of the hematite photoanode resulting in high density of oxygen vacancies exhibited high PEC water oxidation activity reaching a photocurrent of 2.03 mA/cm^2 at 1.23 V vs RHE under a 500 W Xe lamp (285 mW/cm^2) illumination. This photocurrent is 12 times higher than that of the as-prepared hematite without plasma treatment. The improved PEC performance was attributed to the introduction of oxygen vacancies, which lower the adsorption energy of H_2O and increase the carrier density. This work not only adopts low temperature annealing to obtain hematite nanoflakes but also develops a simple strategy to introduce oxygen vacancies for the promotion of water splitting efficiency. The intentional control of the oxygen vacancy density realized using a plasma treatment is thought to be applicable to other hematite nanostructures and metal oxide materials which could be used to improve PEC performance.

ASSOCIATED CONTENT

Supporting Information

The Supporting Information is available free of charge on the ACS Publications website at DOI: 10.1021/acsami.5b06131.

Figures S1−S9 and Table S1 (PDF)

AUTHOR INFORMATION

Corresponding Author

*E-mail: jean@mech.t.u-tokyo.ac.jp.

DOI: 10.1021/acsami.5b06131
ACS Appl. Mater. Interfaces 2015, 7, 22355−22363

Author Contributions

[#]C.Z. and C.L. contributed equally.

Notes

The authors declare no competing financial interest.

■ ACKNOWLEDGMENTS

Parts of this work were supported by "Nanotechnology Platform" (project no. 12024046) of the Ministry of Education, Culture, Sports, Science and Technology (MEXT), Japan and by the JSPS Core-to-Core program (Advanced Research Networks type A). C.Z. and C.L. acknowledge support from the China Scholarship Council (201406230182 and 201206230077).

■ REFERENCES

(1) Grätzel, M. Photoelectrochemical Cells. *Nature* **2001**, *414*, 338−344.
(2) Walter, M. G.; Warren, E. L.; McKone, J. R.; Boettcher, S. W.; Mi, Q.; Santori, E. A.; Lewis, N. S. Solar Water Splitting Cells. *Chem. Rev.* **2010**, *110*, 6446−6473.
(3) Li, C.; Hisatomi, T.; Watanabe, O.; Nakabayashi, M.; Shibata, N.; Domen, K.; Delaunay, J.-J. Positive Onset Potential and Stability of Cu_2O-based Photocathodes in Water Splitting by Atomic Layer Deposition of a Ga_2O_3 Buffer Layer. *Energy Environ. Sci.* **2015**, *8*, 1493−1500.
(4) Sivula, K.; Le Formal, F.; Grätzel, M. Solar Water Splitting: Progress Using Hematite (α-Fe_2O_3) Photoelectrodes. *ChemSusChem* **2011**, *4*, 432−449.
(5) Tilley, S. D.; Cornuz, M.; Sivula, K.; Grätzel, M. Light-Induced Water Splitting with Hematite: Improved Nanostructure and Iridium Oxide Catalysis. *Angew. Chem., Int. Ed.* **2010**, *49*, 6405−6408.
(6) Zhang, Y.; Jiang, S.; Song, W.; Zhou, P.; Ji, H.; Ma, W.; Hao, W.; Chen, C.; Zhao, J. Nonmetal P-doped Hematite Photoanode with Enhanced Electron Mobility and High Water Oxidation Activity. *Energy Environ. Sci.* **2015**, *8*, 1231−1236.
(7) Kim, J. Y.; Magesh, G.; Youn, D. H.; Jang, J. W.; Kubota, J.; Domen, K.; Lee, J. S. Single-crystalline, Wormlike Hematite Photoanodes for Efficient Solar Water Splitting. *Sci. Rep.* **2013**, *3*, 2681.
(8) Forster, M.; Potter, R. J.; Ling, Y.; Yang, Y.; Klug, D. R.; Li, Y.; Cowan, A. J. Oxygen Deficient α-Fe_2O_3 Photoelectrodes: A Balance between Enhanced Electrical Properties and Trap-mediated Losses. *Chem. Sci.* **2015**, *6*, 4009−4016.
(9) Sivula, K.; Zboril, R.; Le Formal, F.; Robert, R.; Weidenkaff, A.; Tucek, J.; Frydrych, J.; Grätzel, M. Photoelectrochemical Water Splitting with Mesoporous Hematite Prepared by a Solution-Based Colloidal Approach. *J. Am. Chem. Soc.* **2010**, *132*, 7436−7444.
(10) Dotan, H.; Kfir, O.; Sharlin, E.; Blank, O.; Gross, M.; Dumchin, I.; Ankonina, G.; Rothschild, A. Resonant Light Trapping in Ultrathin Films for Water Splitting. *Nat. Mater.* **2013**, *12*, 158−164.
(11) Klahr, B. M.; Hamann, T. W. Current and Voltage Limiting Processes in Thin Film Hematite Electrodes. *J. Phys. Chem. C* **2011**, *115*, 8393−8399.
(12) Hisatomi, T.; Dotan, H.; Stefik, M.; Sivula, K.; Rothschild, A.; Grätzel, M.; Mathews, N. Enhancement in the Performance of Ultrathin Hematite Photoanode for Water Splitting by an Oxide Underlayer. *Adv. Mater.* **2012**, *24*, 2699−2702.
(13) Le Formal, F.; Grätzel, M.; Sivula, K. Controlling Photoactivity in Ultrathin Hematite Films for Solar Water-Splitting. *Adv. Funct. Mater.* **2010**, *20*, 1099−1107.
(14) Price, M. J.; Maldonado, S. Macroporous n-GaP in Nonaqueous Regenerative Photoelectrochemical Cells. *J. Phys. Chem. C* **2009**, *113*, 11988−11994.
(15) Liu, C.; Sun, J.; Tang, J.; Yang, P. Zn-Doped p-Type Gallium Phosphide Nanowire Photocathodes from a Surfactant-Free Solution Synthesis. *Nano Lett.* **2012**, *12*, 5407−5411.
(16) Zhu, C.; Zheng, M.; Xiong, Z.; Li, H.; Shen, W. Electrochemically Etched Triangular Pore Arrays on GaP and Their photoelectrochemical Properties from Water Oxidation. *Int. J. Hydrogen Energy* **2014**, *39*, 10861−10869.
(17) Brillet, J.; Grätzel, M.; Sivula, K. Decoupling Feature Size and Functionality in Solution-Processed, Porous Hematite Electrodes for Solar Water Splitting. *Nano Lett.* **2010**, *10*, 4155−4160.
(18) Ling, Y.; Wang, G.; Wheeler, D. A.; Zhang, J. Z.; Li, Y. Sn-Doped Hematite Nanostructures for Photoelectrochemical Water Splitting. *Nano Lett.* **2011**, *11*, 2119−2125.
(19) Wang, L.; Lee, C. Y.; Mazare, A.; Lee, K.; Müller, J.; Spiecher, E.; Schmuki, P. Enhancing the Water Splitting Efficiency of Sn-Doped Hematite Nanoflakes by Flame Annealing. *Chem. - Eur. J.* **2014**, *20*, 77−82.
(20) Lin, Y.; Zhou, S.; Sheehan, S. W.; Wang, D. Nanonet-Based Hematite Heteronanostructures for Efficient Solar Water Splitting. *J. Am. Chem. Soc.* **2011**, *133*, 2398−2401.
(21) Cesar, I.; Sivula, K.; Kay, A.; Zboril, R.; Grätzel, M. Influence of Feature Size, Film Thickness, and Silicon Doping on the Performance of Nanostructured Hematite Photoanodes for Solar Water Splitting. *J. Phys. Chem. C* **2009**, *113*, 772−782.
(22) Satsangi, V. R.; Kumari, S.; Singh, A. P.; Shrivastav, R.; Dass, S. Nanostructured Hematite for Photoelectrochemical Generation of Hydrogen. *Int. J. Hydrogen Energy* **2008**, *33*, 312−318.
(23) Jang, J. S.; Lee, J.; Ye, H.; Fan, F. R. F.; Bard, A. J. Rapid Screening of Effective Dopants for Fe_2O_3 Photocatalysts with Scanning Electrochemical Microscopy and Investigation of Their Photoelectrochemical Properties. *J. Phys. Chem. C* **2009**, *113*, 6719−6724.
(24) Hahn, N. T.; Mullins, C. B. Photoelectrochemical Performance of Nanostructured Ti- and Sn-Doped α-Fe_2O_3 Photoanodes. *Chem. Mater.* **2010**, *22*, 6474−6482.
(25) Glasscock, J. A.; Barnes, P. R. F.; Plumb, I. C.; Savvides, N. Enhancement of Photoelectrochemical Hydrogen Production from Hematite Thin Films by the Introduction of Ti and Si. *J. Phys. Chem. C* **2007**, *111*, 16477−16488.
(26) Sartoretti, C. J.; Alexander, B. D.; Solarska, R.; Rutkowska, I. A.; Augustynski, J.; Cerny, R. Photoelectrochemical Oxidation of Water at Transparent Ferric Oxide Film Electrodes. *J. Phys. Chem. B* **2005**, *109*, 13685−13692.
(27) Warwick, M. E. A.; Barreca, D.; Bontempi, E.; Carraro, G.; Gasparotto, A.; Maccato, C.; Kaunisto, K.; Ruoko, T. P.; Lemmetyinen, H.; Sada, C.; Gönüllü, Y.; Mathur, S. Pt-functionalized Fe_2O_3 Photoanodes for Solar Water Splitting: the Role of Hematite Nano-organization and the Platinum Redox State. *Phys. Chem. Chem. Phys.* **2015**, *17*, 12899−12907.
(28) Mirbagheri, N.; Wang, D.; Peng, C.; Wang, J.; Huang, Q.; Fan, C.; Ferapontova, E. E. Visible Light Driven Photoelectrochemical Water Oxidation by Zn- and Ti-Doped Hematite Nanostructures. *ACS Catal.* **2014**, *4*, 2006−2015.
(29) Lei, F.; Sun, Y.; Liu, K.; Gao, S.; Liang, L.; Pan, B.; Xie, Y. Oxygen Vacancies Confined in Ultrathin Indium Oxide Porous Sheets for Promoted Visible-Light Water Splitting. *J. Am. Chem. Soc.* **2014**, *136*, 6826−6829.
(30) Bao, J.; Zhang, X.; Fan, B.; Zhang, J.; Zhou, M.; Yang, W.; Hu, X.; Wang, H.; Pan, B.; Xie, Y. Ultrathin Spinel-Structured Nanosheets Rich in Oxygen Deficiencies for Enhanced Electrocatalytic Water Oxidation. *Angew. Chem., Int. Ed.* **2015**, *54*, 7399−7404.
(31) Ling, Y.; Wang, G.; Wang, H.; Yang, Y.; Li, Y. Low-Temperature Activation of Hematite Nanowires for Photoelectrochemical Water Oxidation. *ChemSusChem* **2014**, *7*, 848−853.
(32) Gan, J.; Lu, X.; Wu, J.; Xie, S.; Zhai, T.; Yu, M.; Zhang, Z.; Mao, Y.; Wang, S. C.; Shen, Y.; Tong, Y. Oxygen Vacancies Promoting Photoelectrochemical Performance of In_2O_3 Nanocubes. *Sci. Rep.* **2013**, *3*, 1021.
(33) Moir, J.; Soheilnia, N.; Liao, K.; O'Brien, P.; Tian, Y.; Burch, K. S.; Ozin, G. A. Activation of Ultrathin Films of Hematite for Photoelectrochemical Water Splitting via H_2 Treatment. *ChemSusChem* **2015**, *8*, 1557−1567.

DOI: 10.1021/acsami.5b06131
ACS Appl. Mater. Interfaces 2015, 7, 22355−22363

(34) Yang, T. Y.; Kang, H. Y.; Sim, U.; Lee, Y. J.; Lee, J. H.; Koo, B.; Nam, K. T.; Joo, Y. C. A New Hematite Photoanode Doping Strategy for Solar Water Splitting: Oxygen Vacancy Generation. *Phys. Chem. Chem. Phys.* **2013**, *15*, 2117−2124.
(35) Ling, Y.; Wang, G.; Reddy, J.; Wang, C.; Zhang, J. Z.; Li, Y. The Influence of Oxygen Content on the Thermal Activation of Hematite Nanowires. *Angew. Chem., Int. Ed.* **2012**, *51*, 4074−4079.
(36) Li, Y.; Zhang, L.; Torres-Pardo, A.; González-Calbet, J. M.; Ma, Y.; Oleynikov, P.; Terasaki, O.; Asahina, S.; Shima, M.; Cha, D.; Zhao, L.; Takanabe, K.; Kubota, J.; Domen, K. Cobalt Phosphate-Modified Barium-Doped Tantalum Nitride Nanorod Photoanode with 1.5% Solar Energy Conversion Efficiency. *Nat. Commun.* **2013**, *4*, 2566.
(37) Kanan, M. W.; Nocera, D. G. In Situ Formation of an Oxygen-Evolving Catalyst in Neutral Water Containing Phosphate and Co^{2+}. *Science* **2008**, *321*, 1072−1075.
(38) Hiralal, P.; Unalan, H. E.; Wijayantha, K. G. U.; Kursumovic, A.; Jefferson, D.; MacManus-Driscoll, J. L.; Amaratunga, G. A. J. Growth and Process Conditions of Aligned and Patternable Films of Iron(III) Oxide Nanowires by Thermal Oxidation of Iron. *Nanotechnology* **2008**, *19*, 455608.
(39) Grigorescu, S.; Lee, C. Y.; Lee, K.; Albu, S.; Paramasivam, I.; Demetrescu, I.; Schmuki, P. Thermal Air Oxidation of Fe: Rapid Hematite Nanowire Growth and Photoelectrochemical Water Splitting Performance. *Electrochem. Commun.* **2012**, *23*, 59−62.
(40) Choi, Y.; Shin, S.; Park, D.; Choi, J. Surface Treatment of Iron by Electrochemical Oxidation and Subsequent Annealing for the Improvement of Anti-Corrosive Properties. *Curr. Appl. Phys.* **2014**, *14*, 641−648.
(41) Zong, B.; Wu, Y.; Han, G.; Yang, B.; Luo, P.; Wang, L.; Qiu, J.; Li, K. Synthesis of Iron Oxide Nanostructures by Annealing Electrodeposited Fe-Based Films. *Chem. Mater.* **2005**, *17*, 1515−1520.
(42) Mettenbörger, A.; Singh, T.; Singh, A. P.; Järvi, T. T.; Moseler, M.; Valldor, M.; Mathur, S. Plasma-Chemical Reduction of Iron Oxide Photoanodes for Efficient Solar Hydrogen Production. *Int. J. Hydrogen Energy* **2014**, *39*, 4828−4835.
(43) de Faria, D. L. A.; Venâncio Silva, S.; de Oliveira, M. T. Raman Microspectroscopy of Some Iron Oxides and Oxyhydroxides. *J. Raman Spectrosc.* **1997**, *28*, 873−878.
(44) Desai, J. D.; Pathan, H. M.; Min, S. K.; Jung, K. D.; Joo, O. S. FT-IR, XPS and PEC Characterization of Spray Deposited Hematite Thin Films. *Appl. Surf. Sci.* **2005**, *252*, 1870−1875.
(45) Fujii, T.; de Groot, F. M. F.; Sawatzky, G. A.; Voogt, F. C.; Hibma, T.; Okada, K. In Situ XPS Analysis of Various Iron Oxide Films Grown by NO_2-assisted Molecular-Beam Epitaxy. *Phys. Rev. B: Condens. Matter Mater. Phys.* **1999**, *59*, 3195−3202.
(46) Hu, Y. S.; Kleiman-Shwarsctein, A.; Forman, A. J.; Hazen, D.; Park, J. N.; McFarland, E. W. Pt-Doped α-Fe_2O_3 Thin Films Active for Photoelectrochemical Water Splitting. *Chem. Mater.* **2008**, *20*, 3803−3805.
(47) Lu, J.; Jiao, X.; Chen, D.; Li, W. Solvothermal Synthesis and Characterization of Fe_3O_4 and γ-Fe_2O_3 Nanoplates. *J. Phys. Chem. C* **2009**, *113*, 4012−4017.
(48) Teng, X.; Black, D.; Watkins, N. J.; Gao, Y.; Yang, H. Platinum-Maghemite Core−Shell Nanoparticles Using a Sequential Synthesis. *Nano Lett.* **2003**, *3*, 261−264.
(49) Lu, X.; Wu, D.; Li, R.; Li, Q.; Ye, S.; Tong, Y.; Li, G. Hierarchical NiCo2O4 Nanosheets@Hollow Microrod Arrays for High-Performance Asymmetric Supercapacitors. *J. Mater. Chem. A* **2014**, *2*, 4706−4713.
(50) Choudhury, T.; Saied, S. O.; Sullivan, J. L.; Abbot, A. M. Reduction of Oxides of Iron, Cobalt, Titanium and Niobium by Low-Energy Ion Bombardment. *J. Phys. D: Appl. Phys.* **1989**, *22*, 1185−1195.
(51) Janowitz, C.; Scherer, V.; Mohamed, M.; Krapf, A.; Dwelk, H.; Manzke, R.; Galazka, Z.; Uecker, R.; Irmacher, K.; Fornari, R.; Michling, M.; Scheisser, D.; Weber, J. R.; Varley, J. B.; Van de Walle, C. G. Experimental Electronic Structure of In_2O_3 and Ga_2O_3. *New J. Phys.* **2011**, *13*, 085014.
(52) Shinar, R.; Kennedy, J. H. Photoactivity of Doped α-Fe_2O_3 Electrodes. *Sol. Energy Mater.* **1982**, *6*, 323−335.
(53) Kennedy, J. H.; Frese, K. W. Photooxidation of Water at α-Fe_2O_3 Electrodes. *J. Electrochem. Soc.* **1978**, *125*, 709−714.
(54) Li, C.; Li, Y.; Delaunay, J.-J. A Novel Method to Synthesize Highly Photoactive Cu_2O Microcrystalline Films for Use in Photoelectrochemical Cells. *ACS Appl. Mater. Interfaces* **2014**, *6*, 480−486.
(55) Wilkinson, F. Diffuse Reflectance Flash Photolysis. *J. Chem. Soc., Faraday Trans. 2* **1986**, *82*, 2073−2081.
(56) Abdi, F. F.; van de Krol, R. Nature and Light Dependence of Bulk Recombination in Co-Pi-Catalyzed $BiVO_4$ Photoanodes. *J. Phys. Chem. C* **2012**, *116*, 9398−9404.
(57) Surendranath, Y.; Dincă, M.; Nocera, D. G. Electrolyte-Dependent Electrosynthesis and Activity of Cobalt-Based Water Oxidation Catalysts. *J. Am. Chem. Soc.* **2009**, *131*, 2615−2620.
(58) Le Formal, F.; Tétreault, N.; Cornuz, M.; Moehl, T.; Grätzel, M.; Sivula, K. Passivating Surface States on Water Splitting Hematite Photoanodes with Alumina Overlayers. *Chem. Sci.* **2011**, *2*, 737−743.
(59) Kennedy, J.; Frese, K. Flatband Potentials and Donor Densities of Polycrystalline α-Fe_2O_3 Determined from Mott-Schottky Plots. *J. Electrochem. Soc.* **1978**, *125*, 723−726.
(60) Mora-Seró, I.; Fabregat-Santiago, F.; Denier, B.; Bisquert, J.; Tena-Zaera, R.; Elias, J.; Lévy-Clément, C. Determination of carrier density of ZnO nanowires by electrochemical techniques. *Appl. Phys. Lett.* **2006**, *89*, 203117.
(61) Li, H.; Zheng, M.; Liu, S.; Ma, L.; Zhu, C.; Xiong, Z. Reversible Surface Wettability Transition between Superhydrophobicity and Superhydrophilicity on Hierarchical Micro/Nanostructure ZnO Mesh Films. *Surf. Coat. Technol.* **2013**, *224*, 88−92.
(62) Sun, R. D.; Nakajima, A.; Fujishima, A.; Watanabe, T.; Hashimoto, K. Photoinduced Surface Wettability Conversion of ZnO and TiO_2 Thin Films. *J. Phys. Chem. B* **2001**, *105*, 1984−1990.

DOI: 10.1021/acsami.5b06131
ACS Appl. Mater. Interfaces 2015, 7, 22355−22363